

## **DESIGN AND ANALYSIS OF HIGH-VOLTAGE HIGH-EFFICIENCY ULTRA-WIDEBAND PULSE SYNTHESIZER**

**C. Fang and C. L. Law**

PWTC Center  
Nanyang Technological University  
Singapore 639815, Singapore

**J. C. M. Hwang**

Lehigh University  
Bethlehem, PA 18015, USA

**J. Xia**

PWTC Center  
Nanyang Technological University  
Singapore 639815, Singapore

**Abstract**—A novel ultra-wideband (UWB) pulse synthesizer is proposed, which uses a distributed amplifier to combine Gaussian pulses of different polarities, amplitudes and delays. The center frequency and bandwidth of the synthesized pulse can be adjusted by varying the number of the Gaussian pulses and the delays between them. Compared to other UWB pulse generators, the present synthesizer is capable of higher voltages and higher efficiencies. Using 0.25- $\mu\text{m}$  pHEMTs, a prototype synthesizer has been designed and fabricated with a center frequency of 4.0 GHz and a bandwidth of 1.9 GHz. Under a Gaussian input pulse of 1.5 V and 100 ps, the synthesizer outputs into 50  $\Omega$  a pulse of 4.5 V and 1 ns. At a pulse-repetition frequency of 10 MHz, the synthesizer consumes 1 mA at 3 V with 17% efficiency. Approaches to maintain high efficiency by scaling the supply voltage for different input amplitudes and pulse-repetition frequencies have also been verified experimentally.

## 1. INTRODUCTION

Ultra-wideband (UWB) impulse radio [1] has received considerable interest recently. One of its major applications is long-range low-data-rate communication with precision localization [2]. For this application, it is critical to generate UWB pulses with high voltage and high efficiency at low pulse-repetition frequency (PRF) while complying with spectrum regulations. Worldwide, there are many different UWB standards. The U. S. Federal Communications Commission (FCC) has allocated the 3.1–10.6 GHz band with 3–5 GHz being the low band and 6–10 GHz being the high band [3]. This paper focuses on the low band for its superior propagating characteristics.

Traditionally, there are six major methods to generate UWB pulses. One method is to generate a pulse at the baseband then up-convert it to the UWB band [4]. Such a carrier-based design tends to have complex architecture and high power consumption. Also, it requires a local oscillator, which signal can leak into the output. The second method is to generate a pulse directly in the UWB band [5]. This method usually requires more pulse-shaping filters. The third method is to synthesize the pulse waveform by using high-speed digital-to-analog converters [6]. It has both good time and amplitude resolutions, but the high sampling rate increases circuit complexity, power consumption and cost. The fourth method relies on the combination of the rising and falling edges of a clock signal [7]. The fifth method combines different delay edges with polarity control to form a short logic pulse before filtering it [8]. None of the third, fourth and fifth methods can generate high-voltage pulses. In comparison, the sixth method based on an  $L$ - $C$  voltage-controlled oscillator (VCO) can generate a high-voltage pulse [9]. However, the fast gate bias signal required to switch the buffer driver amplifier is difficult to be implemented. Table 1 compares the amplitude, width and efficiency of UWB pulses generated by the different methods. The amplitude is measured peak to peak. The width is the full width at half maximum. The efficiency is defined as

$$\eta = \frac{\text{Peak Output Power} \times \text{Pulse Width} \times \text{PRF}}{\text{DC Power Consumption}}. \quad (1)$$

Recently, we proposed [10] a variation from the fifth method by using a distributed amplifier to combine Gaussian pulses of different polarities, amplitudes and delays. The Gaussian input pulses were generated [11] directly from the rising edges of a clock signal without additional power consumption. The positive pulses are generated from reflected negative pulses without additional polarity-control circuit. As listed in Table 1, from a 1.5-V 100-ps Gaussian input pulse, the new

**Table 1.** Characteristics of UWB pulses generated by difference methods.

Amplitude (V)	Width (ns)	Efficiency	PRF (MHz)	Reference
0.26	1.5	—	—	[4]
0.5	—	—	—	[6]
0.68	0.25	0.94%	500	[7]
0.2	0.6	0.05%	80	[8]
5.1 <sup>a</sup>	0.9	7.9%	1	[9]
4.5	1.0	10%	10	[10]
4.5	1.0	17%	10	This Work
6.4	1.0	13%	5	

<sup>a</sup> Converted from 100-Ω load to 50-Ω load.

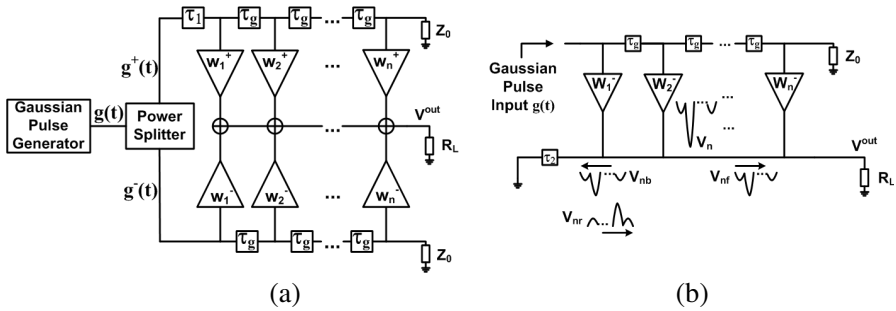


**Figure 1.** Schematics of (a) original and (b) simplified UWB pulse synthesizer.

method could output into 50 Ω a 4.5-V 1-ns pulse with 10% efficiency under a PRF of 10 MHz. This paper expands on [10] mainly by describing the detailed circuit design and analysis in both time and frequency domains. Approaches to maintain high efficiency by scaling the supply voltage for different input amplitudes and PRFs are also explored. The resulted improvements in both output amplitude and efficiency are listed in Table 1.

## 2. PULSE-SYNTHESIS METHOD

Figure 1(a) shows that the proposed UWB pulse synthesizer is based on a distributed amplifier with two branches and  $n$  taps. First, a Gaussian input pulse  $g(t)$  is divided by a power splitter into two sub-pulses  $g^+(t)$

and  $g^-(t)$ . Second,  $g^+(t)$  is delayed by  $\tau_1$  then distributed to each tap of the distributed amplifier with additional delay  $\tau_g$  and weight  $w_i^+$  ( $w_i^+ > 0$ ). In contrast,  $g^-(t)$  is directly distributed to each tap with only tap-to-tap delay  $\tau_g$  and is weighted by  $w_i^-$  ( $w_i^- < 0$ ). Both  $g^+(t)$  and  $g^-(t)$  are terminated in matched loads to prevent reflection. Lastly, the output pulse is synthesized by combining pulses from both the positive and negative branches of the distributed amplifier as

$$V_n^{out}(t) = \sum_{i=1}^n \{w_i^+ g^+[t - \tau_1 - (i-1)\tau_g] + w_i^- g^-[t - (i-1)\tau_g]\} \quad (2)$$

Assuming ideal splitter and equal weights so that  $g^+(t) = g^-(t) = g(t)/\sqrt{2}$ ,  $w_i^+ = 1$  and  $w_i^- = -1$ , (2) can be simplified as

$$V_n^{out}(t) = \frac{1}{\sqrt{2}} \sum_{i=1}^n \{g[t - \tau_1 - (i-1)\tau_g] - g[t - (i-1)\tau_g]\}. \quad (3)$$

The values of  $\tau_1$ ,  $\tau_g$  and  $n$  can be adjusted to optimize the synthesizer performance for different applications. By adjusting  $\tau_1$ , the output center frequency can be tuned. By adjusting  $\tau_g$  and  $n$ , the output width can also be tuned. The adjustments can be analyzed by assuming a Gaussian input pulse of

$$g(t) = \left(A/\sqrt{2\pi\sigma^2}\right) \exp(-t^2/2\sigma^2) \quad (4)$$

where  $A/\sqrt{2\pi\sigma^2}$  is the peak-to-peak amplitude and  $2\sigma\sqrt{2\ln 2}$  is the full width at half maximum. The Fourier transform of (4) in the frequency domain is

$$g(\omega) = A \exp[-\omega^2\sigma^2/2] \quad (5)$$

where  $\omega$  is the angular frequency. From (3)–(5), the output waveform and spectrum can be analyzed for synthesizers with different numbers of taps.

When  $n = 1$ ,

$$\begin{aligned} V_1^{out}(t) &= \left(1/\sqrt{2}\right) [g(t - \tau_1) - g(t)] \\ V_1^{out}(\omega) &= \left[g(\omega)/\sqrt{2}\right] [\exp(-j\omega\tau_1) - 1]. \end{aligned} \quad (6)$$

The corresponding power spectral density is

$$|V_1^{out}(\omega)|^2 = |g(\omega)|^2 2 \sin^2(\omega\tau_1/2). \quad (7)$$

Let  $G_n(\omega)$  be the power gain of an  $n$ -tap synthesizer, then

$$|V_n^{out}(\omega)|^2 = |g(\omega)|^2 G_n(\omega) \quad (8)$$

and

$$G_1(\omega) = 2 \sin^2(\omega\tau_1/2). \quad (9)$$

$G_1(\omega)$  has peaks at  $m\pi/\tau_1$  and nulls at  $(m - 1)\pi/\tau_1$ , where  $m$  is an odd integer. This is the special case when the center frequency and bandwidth are both determined by  $\tau_1$ , because  $\tau_g$  is absent when  $n = 1$ .

When  $n = 2$ ,

$$\begin{aligned} V_2^{out}(t) &= V_1^{out}(t) + V_1^{out}(t - \tau_g) \\ V_2^{out}(\omega) &= V_1^{out}(\omega) [1 + \exp(-j\omega\tau_g)] \\ G_2(\omega) &= 8 \cos^2(\omega\tau_g/2) \sin^2(\omega\tau_1/2) \end{aligned} \quad (10)$$

In addition to peaks at  $m\pi/\tau_1$  and nulls at  $(m - 1)\pi/\tau_1$ ,  $G_2(\omega)$  has nulls at  $m\pi/\tau_g$ . Thus, while the center frequency is determined by  $\tau_1$ , the bandwidth may be determined by  $\tau_g$  if  $\tau_g > \tau_1$ .

When  $n = 3$ ,

$$\begin{aligned} V_3^{out}(t) &= V_1^{out}(t) + V_1^{out}(t - \tau_g) + V_1^{out}(t - 2\tau_g) \\ V_3^{out}(\omega) &= V_1^{out}(\omega) [1 + \exp(-j\omega\tau_g) + \exp(-j2\omega\tau_g)] \\ G_3(\omega) &= 2 [1 + 2 \cos(\omega\tau_g)]^2 \sin^2(\omega\tau_1/2) \end{aligned} \quad (11)$$

In addition to peaks at  $m\pi/\tau_1$  and nulls at  $(m - 1)\pi/\tau_1$ ,  $G_3(\omega)$  has nulls at  $2(m \pm 1/3)\pi/\tau_g$ .

When  $n = 4$ ,

$$\begin{aligned} V_4^{out}(t) &= V_1^{out}(t) + V_1^{out}(t - \tau_g) + V_1^{out}(t - 2\tau_g) + V_1^{out}(t - 3\tau_g) \\ V_4^{out}(\omega) &= V_1^{out}(\omega) \left[ \begin{array}{l} 1 + \exp(-j\omega\tau_g) \\ + \exp(-j\omega 2\tau_g) + \exp(-j\omega 3\tau_g) \end{array} \right] \\ G_4(\omega) &= 32 \cos^2(\omega\tau_g) \cos^2(\omega\tau_g/2) \sin^2(\omega\tau_1/2) \end{aligned} \quad (12)$$

In addition to peaks at  $m\pi/\tau_1$  and nulls at  $(m - 1)\pi/\tau_1$ ,  $G_4(\omega)$  has nulls at  $m\pi/2\tau_g$  and  $m\pi/4\tau_g$ .

Thus, the output spectra of synthesizers with different numbers of taps can be evaluated by using (9)–(12). To illustrate the cases for  $\tau_g > \tau_1$ ,  $\tau_g$  is fixed at  $2\tau_1$ . Fig. 2(a) plots gains  $G_1(\omega)$ ,  $G_2(\omega)$ ,  $G_3(\omega)$ , and  $G_4(\omega)$  for  $\tau_1 = 120$  ps and  $\tau_g = 240$  ps. It can be seen that the bandwidth decreases with increasing  $n$ , so that the output energy is concentrated more in the main lobe and less in the side lobes. For example, with  $n = 4$ , the main lobe is approximately 13 dB higher than its nearest side lobe. With  $n = 4$  and  $\tau_g = 2\tau_1$ , Fig. 2(b) shows that the peak frequency and bandwidth are both inversely proportional to  $\tau_1$ . Table 2 summarizes the peak frequency and 10-dB bandwidth for different  $\tau_1$  values.

According to (8), the output spectrum is determined by not only the synthesizer gain  $G(\omega)$ , but also the shape of the input pulse  $g(\omega)$ .

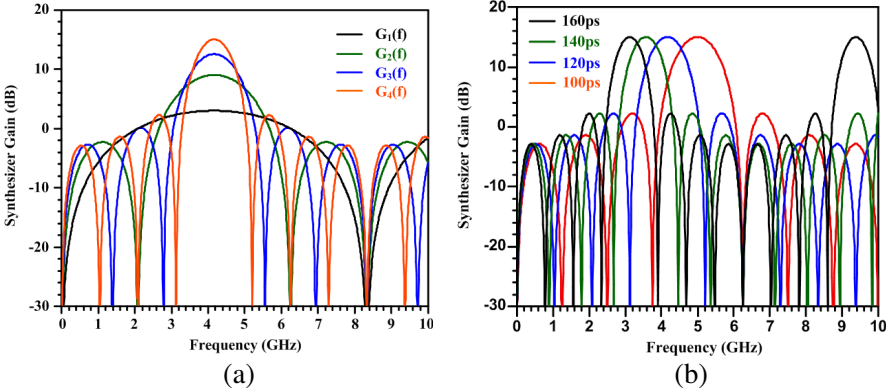


**Figure 2.** Calculated synthesizer gain with (a)  $\tau_1 = 120$  ps and  $n = 1, 2, 3, 4$  and (b)  $n = 4$  and  $\tau_1 = 100, 120, 140, 160$  ps. In all case,  $\tau_g = 2\tau_1$ .

**Table 2.** Characteristics of the synthesizer gain for different delays<sup>a</sup>.

Delay $\tau_1$ (ps)	100	120	140	160
Peak Frequency (GHz)	5.0	4.2	3.6	3.1
Bandwidth (GHz)	1.8	1.5	1.3	1.2

<sup>a</sup> $\tau_g = \tau_1, n = 4$ .

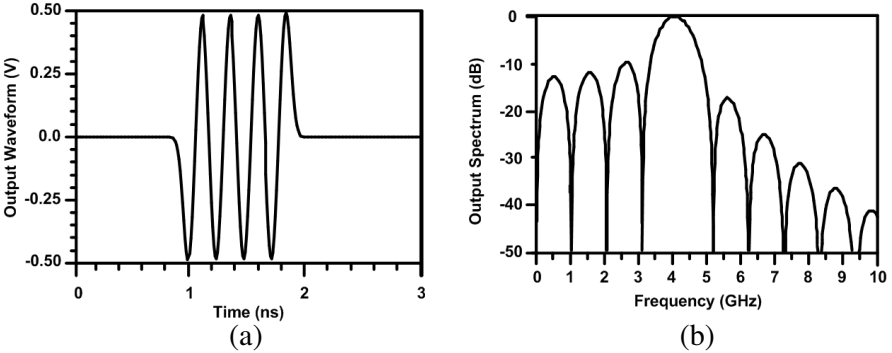


**Figure 3.** Calculated synthesizer output (a) waveform and (b) spectrum with  $n = 4, \tau_1 = 120$  ps,  $\tau_g = 240$  ps, and  $\sigma = 100$  ps.

Using (12), Fig. 3 shows the calculated output waveform and spectrum for  $n = 4, \tau_1 = 120$  ps,  $\tau_g = 240$  ps, and  $\sigma = 100$  ps with the peak-to-peak amplitude in the time domain normalized to 1 V and the main

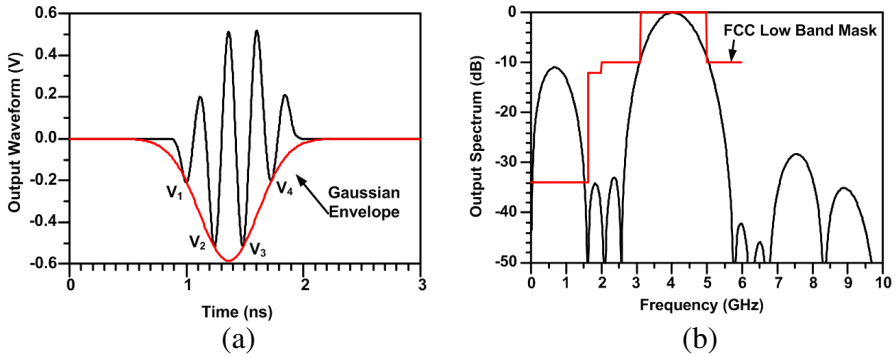


**Figure 4.** Calculated (a) waveform and (b) spectrum of the output pulse with a Gaussian envelope formed by varying the weights  $w_i^+$  and  $w_i^-$  of the distributed amplifier. The FCC spectral mask is overlaid in (b) as a reference.

lobe in the frequency domain normalized to 0 dB. Compared to Fig. 2, the difference between the main lobe and the nearest side lobe is now reduced from 13 dB to 10 dB by the rich low-frequency content of the Gaussian input pulse. In order to utilize the spectral mask more efficiently, the side lobes can be suppressed by adjusting the weights  $w_i^+$  and  $w_i^-$  of the distributed amplifier so that the output pulse follows a Gaussian envelope in the time domain as shown in Fig. 4(a). Fig. 4(b) shows that in this case the main lobe in the frequency domain is more than 30 dB higher than the nearest side lobe. This approach is elaborated in the next section.

### 3. CIRCUIT DESIGN AND ANALYSIS

The proposed distributed UWB pulse synthesizer with a simplified architecture has been implemented in 0.25- $\mu\text{m}$  gate-length depletion-mode pHEMTs, which are biased in Class-C for high-efficiency operation. For the negative branch of the distributed amplifier with  $w_i^-$  weights, each tap is automatically switched on and off by the positive input pulse. However, the positive branch with  $w_i^+$  weights cannot be easily implemented with the depletion-mode pHEMTs in Class-C operation. To overcome the difficulty, the power splitter and the positive branch of the distributed amplifier are eliminated and, instead, positive pulses are generated from reflected negative pulses. As shown in Fig. 1(b), in the simplified architecture, a negative pulse  $V_n$  is first formed by combining the pulses through the negative taps with  $w_i^-$

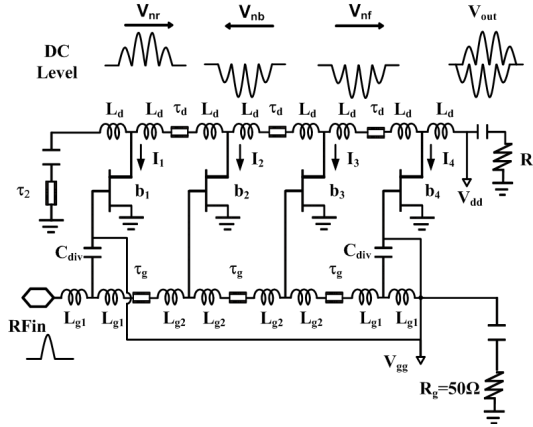


**Figure 5.** Circuit schematic of the simplified UWB pulse synthesizer with one branch and four taps.

weights. The  $V_n$  pulse then travels both forward and backward as indicated by  $V_{nf}$  and  $V_{nb}$ . When the backward traveling  $V_{nb}$  passes through the delay element  $\tau_2$  to reach the short-circuited termination, a positive  $V_{nr}$  is reflected. The reflected pulse  $V_{nr}$  then travels forward to combine with  $V_{nf}$  to form an UWB pulse with both positive and negative components at the output of the distributed amplifier. Note that  $V_{nr}$  is behind  $V_{nf}$  by  $2\tau_1$ . Therefore, the analysis of Section 2 is still valid provided  $\tau_1$  is replaced by  $2\tau_2$ .

Figure 5 shows the circuit design based on the simplified architecture of Fig. 1(b) with  $n = 4$ . A conventional distributed amplifier [12] is implemented with discrete pHEMTs on a combination of ceramic and polymer boards. The typical 50- $\Omega$  termination on the drain side of the pHEMTs is replaced by a short-circuited termination after a transmission line with delay  $\tau_2$ . A short transmission line with delay  $\tau_d$  meanders between the pHEMT drains, while a long transmission line with delay  $\tau_g$  meanders between the pHEMT gates. As described in Section 2, the input pulse travels through  $\tau_g$  and switches the pHEMTs successively, before being absorbed by a 50- $\Omega$  termination. The  $w_i^-$  weights are implemented with voltage dividers made of  $C_{div}$  and  $C_{gs}$  in series, where  $C_{gs}$  is the gate-source capacitance of each pHEMT. Bond wires  $L_{g1}$ ,  $L_{g2}$  and  $L_d$  connect the pHEMTs with the transmission lines on the board and help compensate  $C_{div}$ ,  $C_{gs}$  and  $C_{ds}$  to maintain the 50- $\Omega$  characteristic impedance, where  $C_{ds}$  is the drain-source capacitance of each pHEMT.

The  $C_{div}/C_{gs}$  dividers are designed to give the proper  $w_i^-$  weights

to ensure a Gaussian envelope for efficient spectrum utilization as discussed at the end of Section 2. As shown in Fig. 4(a), four successive positive pulses of amplitudes  $V_1 = V_4$ ,  $V_2 = V_3 = 2.5V_1$  and four successive negative pulses of the same amplitudes but  $180^\circ$  out of phase form an output pulse with a Gaussian envelope. For the present pHEMTs,  $C_{gs} = 0.38$  pF. Therefore,  $C_{div} = 0.25$  pF would give  $V_2 = 2.5V_1$ .

Giving the  $C_{div}/C_{gs}$  ratio, it is tempting to simply let  $w_1^- = w_4^- = -0.4$  and  $w_2^- = w_3^- = -1$ . However, the  $w_i^-$  values can only be determined after considering the transistor gain and parasitic loss. This is accomplished by analyzing the detailed circuit schematic of Fig. 6(b), which is formed by inserting the linear pHEMT model of Fig. 6(a) into Fig. 5. In the analysis, the bond wires  $L_{g1}$ ,  $L_{g2}$  and  $L_d$ , as well as the transmission lines  $\tau_2$  and  $\tau_d$ , are assumed to be lossless. The loss  $Loss_g$  associated with  $\tau_g$  is estimated to be 0.35 dB. The loss associated with the channel resistance  $R_i$  is considered, but the loss associated with the drain-source resistance  $R_{ds}$  is neglected. Delays other than  $\tau_d$  and  $\tau_g$  are all ignored.

With  $V_{gg} = -1.0$  V, each pHEMT is biased below its threshold voltage of  $V_{th} = -0.8$  V and the effective input voltage  $V_{eff}$  under an input pulse of  $V_{in} = 1.5$  V is

$$\begin{aligned}
 V_{eff1} &= \frac{(V_{in} + V_{gg} - V_{th})/j\omega C_{gs}}{1/j\omega C_{gs} + 1/j\omega C_{div} + R_i} = 0.52\text{V} \\
 V_{eff2} &= \frac{(V_{in} + V_{gg} - V_{th})/j\omega C_{gs}}{10^{Loss_g/20} (1/j\omega C_{gs} + R_i)} = 1.44\text{V} \\
 V_{eff3} &= \frac{(V_{in} + V_{gg} - V_{th})/j\omega C_{gs}}{10^{2Loss_g/20} (1/j\omega C_{gs} + R_i)} = 1.20\text{V} \\
 V_{eff4} &= \frac{(V_{in} + V_{gg} - V_{th})/j\omega C_{gs}}{10^{3Loss_g/20} (1/j\omega C_{gs} + 1/j\omega C_{div} + R_i)} = 0.46\text{V}
 \end{aligned} \tag{13}$$

With the transconductance  $g_m = 80$  ms, the current through each pHEMT is 42 mA, 100 mA, 96 mA and 37 mA, respectively. As the drain current is divided between the  $50\text{-}\Omega$  transmission lines left and right, as well as the drain-source resistance  $R_{ds} = 373\ \Omega$ , the effective drain impedance is  $23\ \Omega$ . Therefore, the output voltage for each pHEMT is 0.97 V, 2.34 V, 2.21 V and 0.86 V, which match the measured results of Section 4. From the ratio of output and input voltages on each pHEMT,  $w_1^- = -0.65$ ,  $w_2^- = -1.56$ ,  $w_3^- = -1.50$ , and  $w_4^- = -0.57$ .

By properly combining the output voltage of each pHEMT, the

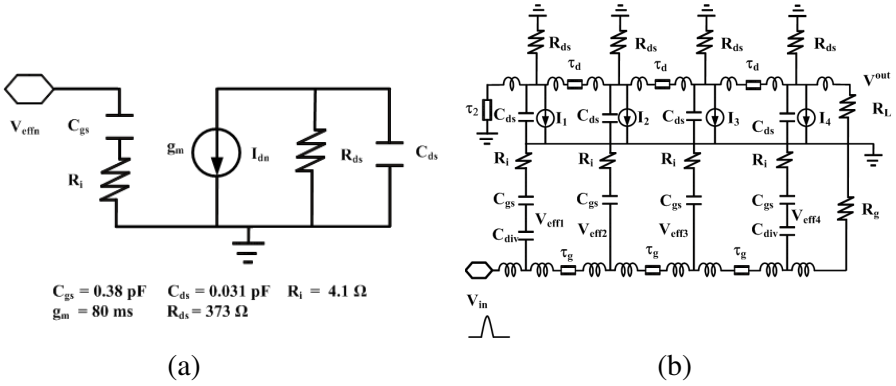


**Figure 6.** (a) Linear pHEMT model and (b) detailed circuit schematic formed by inserting the pHEMT model into the circuit of Fig. 5.

forward traveling pulse at the synthesizer output is

$$\begin{aligned}
 V_{nf}(t) &= w_1^- V_{in}(t - 3\tau_d) + w_2^- V_{in}(t - \tau_g - 2\tau_d) \\
 &\quad + w_3^- V_{in}(t - 2\tau_g - \tau_d) + w_4^- V_{in}(t - 3\tau_g) \\
 V_{nf}(\omega) &= V_{in}(\omega) \cdot \left\{ \begin{aligned} &w_1^- \exp(-j3\omega\tau_d) + w_2^- \exp[-j\omega(\tau_g + 2\tau_d)] \\ &+ w_3^- \exp[-j\omega(2\tau_g + \tau_d)] + w_4^- \exp[-j3\omega\tau_g] \end{aligned} \right\}
 \end{aligned} \quad (14)$$

The backward traveling pulse  $V_{nb}$  can be similarly evaluated knowing that it is of the opposite polarity and is delayed by  $2\tau_2 + 3\tau_d$ . Combining  $V_{nf}$  and  $V_{nb}$ , the output pulse is

$$\begin{aligned}
 V_4^{out}(t) &= V_{nf}(t) - V_{nb}(t - 2\tau_2 - 3\tau_d) \\
 V_4^{out}(\omega) &= V_{nf}(\omega) \{1 - \exp[-j\omega(2\tau_2 + 3\tau_d)]\} \\
 G_4(\omega) &= |1 - \exp[-j\omega(2\tau_2 + 3\tau_d)]|^2 \cdot \left| \begin{aligned} &w_1^- \exp(-j\omega 3\tau_d) + w_2^- \exp[-j\omega(\tau_g + 2\tau_d)] \\ &+ w_3^- \exp[-j\omega(2\tau_g + \tau_d)] + w_4^- \exp(-j\omega 3\tau_g) \end{aligned} \right|^2
 \end{aligned} \quad (15)$$

Equation (15) can be used to calculate the synthesizer gain at any frequency. For example, Fig. 7 shows that with  $\tau_2 = 60$  ps,  $\tau_g = 240$  ps, and  $\tau_d = 15$  ps, the gain calculated by using (15) is in general agreement with that simulated by using the nonlinear TOM3 model [13] for pHEMTs and distributed transmission-line model for the delays. In both cases, the gain at a center frequency of 4.17 GHz is estimated to be 16.5 dB.

Equation (15) differs from (12) in terms of not only  $w_i$ , but also  $\tau_d$ . Fig. 7 shows also the gain calculated by using (15) without  $\tau_d$ .

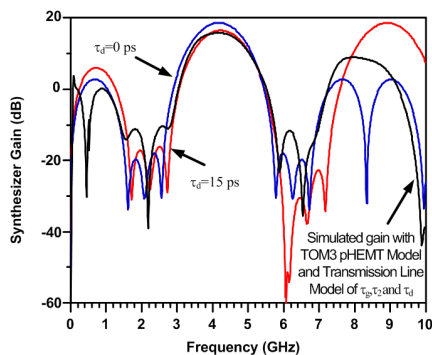


**Figure 7.** Synthesizer gain calculated by using (15) with  $\tau_d = 15$  ps or 0. The calculated gain for  $\tau_d = 15$  ps is in general agreement with that simulated by using TOM3 pHEMT and transmission-line models.

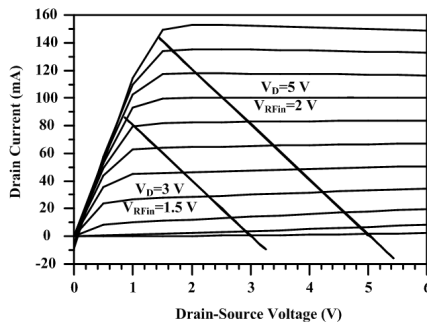


**Figure 8.** Drain characteristics of the pHEMT overlaid with load lines optimized for (a) 1.5-V input with 3-V supply and (b) 2-V input with 5-V supply.

It can be seen that with  $\tau_d$  reduced from 15 ps to 0, the peak gain increases from 16.5 dB to 18.6 dB. This shows that the layout of the distributed amplifier can be further optimized to minimize  $\tau_d$  and to maximize the gain and efficiency of the synthesizer.

Giving the same gain but a lower PRF, the input pulse amplitude can be increased to boost the output pulse amplitude without violating the FCC regulation. With a gain of 16.5 dB and a PRF of 10 MHz, a 1.5-V 100-ps Gaussian input pulse with a spectral density of  $-59$  dBm/MHz at 4.17 GHz would result in an output pulse with  $-42.5$  dBm/MHz at 4.17 GHz, which complies with the FCC regulation and agrees with the measured results of Section 4. If the PRF is reduced from 10 MHz to 5 MHz, the input amplitude can be increased from 1.5 V to 2.0 V to maintain the output spectral density of  $-42.5$  dBm/MHz at 4.17 GHz. However, to maintain the same gain, the supply voltage must also be increased from 3 V to 5 V to accommodate the larger voltage swing as shown in Fig. 8. In general, the supply voltage must be carefully scaled to provide high output amplitude with high linearity and high efficiency. To verify the above analysis, the fabricated synthesizer was tested under different input and supply voltages as described below.

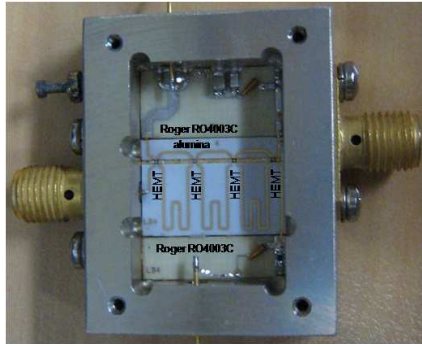


**Figure 9.** Photograph of the fabricated UWB pulse synthesizer.

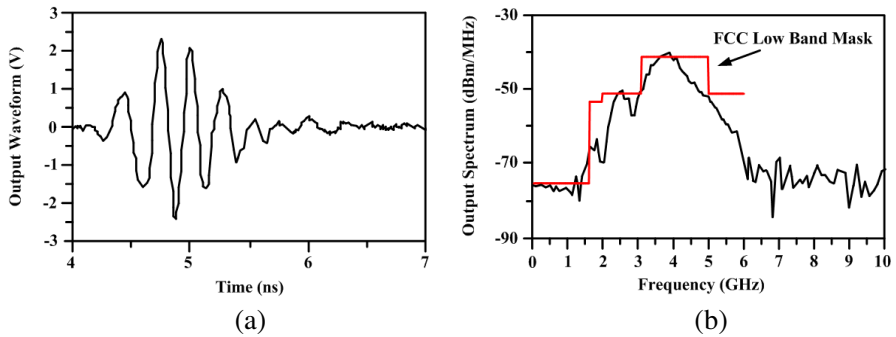
#### 4. RESULTS AND DISCUSSION

Figure 9 is a photograph of a synthesizer fabricated with  $n = 4$ ,  $\tau_2 = 60$  ps,  $\tau_g = 240$  ps, and  $\tau_d = 15$  ps. The circuit size is approximately  $20\text{ mm} \times 30\text{ mm}$ . The delay  $\tau_g$  is through a 29-mm 50- $\Omega$  microstrip line, which meanders over an area of  $4\text{ mm} \times 8\text{ mm}$  on an alumina substrate with a thickness of 0.254 mm and a dielectric constant of 9.9. The delay  $\tau_2$  is through a 9.4 mm 50- $\Omega$  microstrip line with 2.4 mm on the alumina substrate and the remainder on a Roger RO4003C substrate with a thickness of 0.508 mm and a dielectric constant of 3.55. The alumina substrate is more suitable for chip-on-board attachment; the Roger substrate is more suitable for surface-mount components.

The fabricated synthesizer was first tested with a 1.5-V 100-ps Gaussian input and a 10-MHz PRF. As discussed in Section 3, the supply voltage was optimized at 3 V in this case. Fig. 10 shows the measured output waveform and spectrum. The peak-to-peak amplitude is 4.5 V and the full width at half maximum is 1.0 ns. The center frequency and 10-dB bandwidth are 4.0 GHz and 1.9 GHz, respectively, in compliance with the FCC low-band mask. The measured current consumption is 1 mA, which corresponds to an efficiency of 17% as defined by (1).

The same synthesizer was next tested with a 2-V 100-ps Gaussian input and a 5-MHz PRF. Fig. 11 shows the measured output waveform and spectrum. The peak-to-peak voltage is 6.4 V and the full width at half maximum remains at 1.0 ns. The spectrum remains the same in compliance with the FCC mask. The measured current consumption is 0.8 mA, which corresponds to an efficiency of 13%.

As verified in the above, the supply voltage can be scaled to provide high output amplitude with high linearity and high efficiency



**Figure 10.** Measured output (a) waveform and (b) spectrum of the UWB pulse synthesizer with 1.5-V 240-ps Gaussian input, 10-MHz PRF and 3-V supply. The FCC spectral mask is overlaid in (b) as a reference.

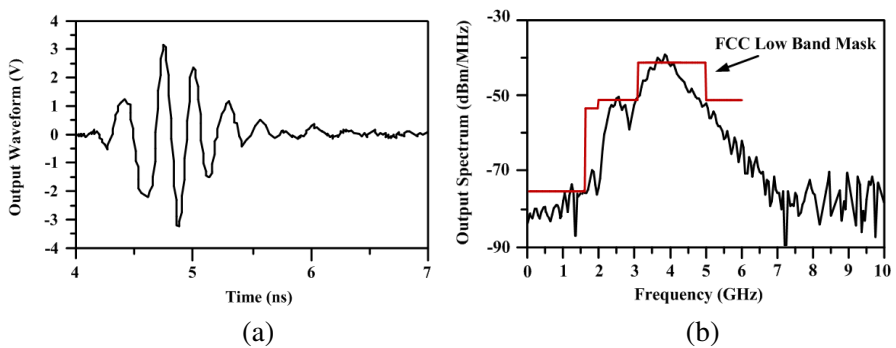


**Figure 11.** Measured output (a) waveform and (b) spectrum of the UWB pulse synthesizer with 1.5-V 240-ps Gaussian input, 10-MHz PRF and 3-V supply. The FCC spectral mask is overlaid in (b) as a reference.

under different input conditions. This can be accomplished by laying out additional circuitry to adjust the input amplitude and PRF for different applications and to adaptively control the supply voltage for the pulse synthesizer according to the chosen input amplitude and PRF. Such adaptive control of the supply voltage has been used to improve the linearity and efficiency of RF power amplifiers [14]. The adaptive control circuitry can be best implemented in monolithically microwave integrated circuits (MMICs).

For expeditious and low-cost proof of concept, the proposed synthesizer was demonstrated by using discrete pHEMTs. Using MMICs, the pulse generator can be integrated with the pulse

synthesizer to facilitate adaptive control of the supply voltage. In addition, parasitic delays such as  $\tau_d$  can be minimized for maximum gain and efficiency. In this case, higher-impedance transmission lines can be used to minimize the die size but must be carefully traded off against additional loss.

## 5. CONCLUSION

The above theoretical analysis and measured results confirm that the proposed distributed UWB pulse synthesizer is capable of higher output amplitude and efficiency than many other UWB pulse generators. In addition, the supply voltage can be adaptively controlled to improve the linearity and efficiency of the proposed synthesizer. Finally, the proposed synthesizer design can be implemented in MMICs for even better performance.

## ACKNOWLEDGMENT

This work was supported in part by Singapore ASTAR SERC under Grant 052-121-0086.

## REFERENCES

1. Win, M. Z. and R. A. Scholtz, "Impulse radio: How it works," *IEEE Commun. Lett.*, Vol. 2, No. 2, 36–38, Feb. 1998.
2. Fontana, R. J., E. Richley, and J. Barney, "Commercialization of an ultra wideband precision asset location system," *Proc. IEEE Int. Conf. Ultra-wideband Systems Technologies*, 369–373, Nov. 2003.
3. Federal Communications Commission, "Revision of part 15 of the commission's rules regarding ultra-wideband transmission systems: First report and order," Washington DC, ET-docket 98-153, FCC 02-48, 1–118, Feb. 14, 2002.
4. Wentzloff, D. D. and A. P. Chandrakasan, "A 3.1–10.6 GHz ultra-wideband pulse shaping mixer," *Proc. IEEE Radio Frequency Integrated Circuits Symp. Dig.*, 83–86, Jun. 2005.
5. Li, K., "Experimental study on UWB pulse generation using UWB band pass filters," *Proc. IEEE Int. Conf. Ultra-wideband Systems Technologies*, 103–108, Sep. 2006.
6. Baranauskas, D. and D. Zelenin, "A 0.36W 6b up to 20GS/s DAC for UWB wave formation," *Proc. IEEE Int. Solid-state Circuits Conf.*, 2380–2389, Feb. 2006.

7. Kim, H., D. Park, and Y. Joo, "All-digital low power CMOS pulse generator for UWB system," *IEE Electronics Lett.*, Vol. 40, No. 24, 1534–1535, Nov. 2004.
8. Smaini, L., et al., "Single-chip CMOS pulse generator for UWB systems," *IEEE J. Solid-state Circuits*, Vol. 41, No. 7, 1551–1561, Jul. 2006.
9. Diao, S. and Y. Zheng, "An ultra low power and high efficiency UWB transmitter for WPAN applications," *Proc. Europe Solid-state Circuit Conf.*, 386–389, Sep. 2008.
10. Fang, C., C. L. Law, and J. C. M. Hwang, "High-voltage high-efficiency ultrawideband pulse synthesizer," *IEEE Microw. Wireless Compon. Lett.*, Vol. 20, 49–51, Jan. 2010.
11. Low, Z. N., J. H. Cheong, and C. L. Law, "Novel low cost higher order derivative Gaussian pulse generator circuit," *Proc. Int. Conf. Communications Systems*, 30–34, Sep. 2004.
12. Strid, E. W. and K. R. Gleeson, "A DC-12 GHz monolithic GaAs FET distributed amplifier," *IEEE Trans. Microw. Theory Tech.*, Vol. 30, No. 7, 969–975, Jul. 1982.
13. TriQuint Semiconductors, Inc., Hillsboro, Oregon, USA.
14. Kimball, D., P. Draxler, J. Jeong, C. Hsia, S. Lanfranco, W. Nagy, K. Linthicum, L. Larson, and P. Asbeck, "50% PAE WCDMA basestation amplifier implemented with GaN HFETs," *IEEE Compound Semiconductor Integrated Circuit Symp. Dig.*, 89–92, Oct. 2005.